THE UNIVERSITY of EDINBURGH

Edinburgh Research Explorer

The effects of wind-induced inclination on the dynamics of semi-submersible floating wind turbines in the time domain

OPEN ACCESS

CrossMark
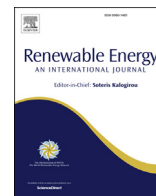
The effects of wind-induced inclination on the dynamics of semi-submersible floating wind turbines in the time domain

Raffaello Antonutti [a, b, c, *], Christophe Peyrard [a, c], Lars Johanning [b, e], Atilla Incecik [b, f], David Ingram [b, d]

[a] EDF R&D — Electricité de France Research and Development, 6 quai Watier, 78400 Chatou, France
[b] Industrial Doctoral Centre for Offshore Renewable Energy, The University of Edinburgh, King's Buildings, Edinburgh EH9 3JL, UK
[c] Saint-Venant Hydraulics Laboratory (EDF, ENPC, Cerema), Université Paris-Est, 6 quai Watier, 78400 Chatou, France
[d] Institute for Energy Systems, School of Engineering, The University of Edinburgh, King's Buildings, Edinburgh EH9 3JL, UK
[e] College of Engineering, Mathematics and Physical Science, Renewable Energy Research Group, University of Exeter, Penryn Campus, Penryn TR10 9EZ, UK
[f] Department of Naval Architecture, Ocean and Marine Engineering, University of Strathclyde, Glasgow G4 0LZ, UK

ARTICLE INFO

ABSTRACT

This study focusses on the coupling effects arising from the changes in the hydrodynamic behaviour of a semi-submersible floating wind turbine when it undergoes large inclinations under wind loading. By means of a range of time-domain simulations, it is shown that both the hull geometric nonlinearity effect and the alteration of viscous hydrodynamic forces can significantly affect the dynamics of a typical floating wind turbine operating in waves at rated conditions. The consequences of said effects for both aligned and misaligned wind and waves are explored. In general terms inclinations are found to increase motions, where the modes that are more affected depend on the relative direction between incident wind and waves. Understanding the sources of aero-hydrodynamic coupling is key to providing sound design and modelling guidelines for the coming generation of floating wind turbines.

© 2015 The Authors. Published by Elsevier Ltd. This is an open access article under the CC BY license (http://creativecommons.org/licenses/by/4.0/).

1. Introduction

In recent years floating wind power has been increasingly regarded as an attractive option for the production of low-carbon electricity, thanks to the potential to unlock vast resources which are unexploitable using fixed substructures; these are expected to become gradually unviable for depths beyond 50–60 m [1,2]. Being able to deploy wind turbines in deep water will be crucial to determine the scale of the industry within regions where the maritime continental shelf is steep. In spite of the presence of vast shallow areas especially in the North Sea, an estimate of the technical resource potential in Europe indicates a deep-water share of about 70% [3]. Estimates for France range between 60% [4] and 80% [3]. In Japan, now a prominent country in floating wind

developments, 80% of the offshore wind resources are located in deep water according to [5].

Different from most conventional offshore floating structures, floating wind turbines (FWTs) are relatively small bodies which can exhibit stronger nonlinearities in their dynamic behaviour. Moreover, they are designed with the purpose of maximising the aerodynamic interaction related to wind energy extraction, which gives rise to unusually large aerodynamic load to displacement ratios. This constitutes an important source of dynamic coupling, especially as FWT platforms tend to evolve toward more optimised, lightweight solutions. Characterising the mechanical behaviour of a floating wind turbine for design and verification purposes requires the coupling of wind turbine aerodynamics and control with offshore hydromechanics. The understanding of such coupled dynamics under complex met-ocean loading has recently been the driver of a novel generation of coupled offshore dynamic models designed for the requirements of FWT mechanical simulation, such as FAST [6–8], HAWC2 [8,9], FloVAWT [10], Simo-Riflex [8,11], and CALHYPSO of EDF R&D, the software used in the present study.

1.1. Small offshore structure hydrodynamics

Compact floating platforms can exhibit increased hydrodynamic complexity when subjected to ocean waves compared to their larger counterparts; for example it is more likely to come across regimes where hydrodynamic drag plays an important part in excitation, as it was observed experimentally on the DeepCwind-OC4 platform by Ref. [12], and explained numerically in Ref. [13]. These phenomena typically affect structures featuring sharp-edged motion control devices, tanks, and pontoons, which accentuate flow separation. Surface proximity effects can also manifest on these appendices when their submergence is limited, such as increased vertical wave loading (conjectured in Ref. [14]) and run-up [15]. As shown by the experimental campaign carried out by Ref. [16] on a CALM buoy equipped with a skirt, a semi-empirical numerical model implementing linear potential diffraction/radiation and a Re-independent drag force formulation can satisfactorily (but not comprehensively, as explained in 1.2) represent the hydrodynamic forces acting on this type of structure for the calculation of dynamic response. Similar conclusions have been drawn by Ref. [17] whilst comparing numerical and experimental motion results for a compact water-injection platform concept, the predecessor of the WindFloat platform design. An analogous numerical-experimental comparison carried out for the engineering design of WindFloat itself broadly confirmed the accuracy of this type of numerical model [2]. Next follows a brief close-up on water entrapment device hydrodynamics and the main related modelling challenges.

1.2. Water entrapment plates

The water entrapment principle, often utilised in the hydrodynamic design of FWTs, provides a passive motion control tool through the installation of relatively low-cost appendices. Pioneered by Principle Power with the WindFloat prototype, the heave plate appendix consists in a thin reinforced structure installed coaxially below the platform's columns, as visible in Fig. 1. The dynamic stability provided by the use of heave plates, coupled with the extra static stability insured by a closed-loop active ballasting system, reportedly allowed the WindFloat prototype to adopt conventional aerogenerator technology [18].

The modelling of water entrapment appendices close to the free surface via linear diffraction and radiation plus a drag model should come with a caveat. As pointed out by Ref. [16], the radiation-dependent vertical added mass of these structures is suspected to

Fig. 1. Detail of a WindFloat prototype column. Photo courtesy of Principle Power.

suffer from the irrotational flow hypothesis (i.e. the model fails to take into account the momentum transfer needed to impel fluid rotation around the edges, causing underestimation of added mass). Another issue consists in the sensitivity of the separation pattern to flow regimes, and in particular to KC [19]. The resulting drag forces — which dominate the hydrodynamic damping for this type of platform — may be affected by such regime changes, thus requiring appropriate adjustments of the drag coefficient. Finally, nonlinearities caused by complex phenomena such as wave decomposition [20] and breaking [21] over the plates may perturb loading in ways that are not captured by the most widespread wave-structure interaction models.

1.3. Large inclinations

One of the routes to FWT CAPEX reduction is the compression of platform fabrication cost. An immediate consequence of this is the push for the minimisation of platform mass and hence size, that in turn entails the availability of smaller displacements and water-plane areas for the sake of hydrostatic stability. Subsequently, low hydrostatic stability platform solutions are currently being proposed. One option is constituted by TLPs (see for example [22]), whose restoring capacity to oppose the aerodynamic overturning forces is built into the mooring system. An alternative approach is simply the acceptance of large-angle operation caused by limited stability, leading to the introduction of the highly compliant FWT concept [23,24]. This, combined with other technological considerations, has caused a range of tilt-tolerant floating VAWT designs to be spawned (see Ref. [25] for a technical discussion and [26] for an industrial application). Although conventional HAWT rotors are known to be tilt-adverse — especially with respect to their aerodynamic efficiency — angles up to $10°$ are beginning to be considered acceptable as the operational limit for this type of turbine (see [27, 28]).

Several widespread assumptions of offshore structure dynamic simulation are challenged by the allowance of relatively large angular displacements. First of all, the ubiquitous hydrostatic linearisation may undermine the correct representation of these forces, especially when the geometry around the waterline is complex and/or hull sides are inclined (see for example the WINFLO concept [29]). The classic static representation of the mass matrix in the inertial frame can also cause errors in the computation of inertial reaction forces as angles break the small displacement assumption. Also, the classic linear superposition of small rotations may prove inaccurate, an observation that has led to the development of FWT motion solvers applying sequential Euler angle changes to represent correctly the nonlinear coupling between motions for a rigid-body [30,31] and a multi-body system [32,33]. Finally, the combination of limited draft, significant inclinations, and the presence of hydrodynamically sensitive appendices — typical of semi-submersible FWTs unequipped with active wind load compensation — has been shown to hold significant potential for the appearance of geometric nonlinearities in the diffraction/radiation behaviour of the hull [34]. The present work builds upon these findings, focussing on the effects of large inclinations on FWT dynamic response due to the alteration of both inertial and viscous hydrodynamic forces. Compared to the preceding work carried out on this subject, in this study a time-domain implementation enables an integral representation of drag forces as well as the inclusion of a coupled, yet simplified, aero-gyroscopic module representing the wind turbine rotor and tower forces.

2. Methodology

A program named CALHYPSO (*CALcul HYdrodynamique Pour les*

Structures Offshore) has been developed at EDF R&D that incorporates the aerodynamic, hydrostatic, hydrodynamic, inertial, and mooring forces exerted on a FWT to resolve its dynamics in the time domain. Whilst HAWT aerodynamics are here represented via a reactive thrust module, CALHYPSO also features a fully-fledged double-multiple streamtube representation of VAWT aerodynamics. This simulation tool has been both verified and validated in the past; simple code-to-code verification examples are available in Ref. [35], whilst the experimental validation of some of the inclination effects described here is scheduled for publication in 2016 (two related articles have been proposed to [36]). The combination of modelling methods adopted in this study, constituting a subset of the CALHYPSO framework, will be explained in the present section.

2.1. Coupled dynamics

The FWT dynamics are implemented using a 6-DoF, rigid body assumption with the reference point O placed at the centre of the structure's waterplane area. Although the choice of this point is entirely arbitrary for the representation of rigid-body dynamics, when floating structures are concerned the above choice of O allows to adopt the widespread metacentric representation of hydrostatic stiffness without incurring in errors. Based on Newton's second law of motion, the EoM of the system are written in the inertial system of reference (SoR) centred in O in the form:

$$(\mathbf{M}+\mathbf{A}^{\infty})\ddot{\mathbf{x}}(t) = \mathbf{f^h}(t)+\mathbf{f^e}(t)+\mathbf{f^r}(t)+\mathbf{f^v}(t)++\mathbf{f^a}(t)+\mathbf{f^g}(t)+\mathbf{f^m}(t), \tag{1}$$

where $\mathbf{M}$ denotes the rigid body's generalised inertia matrix, $\mathbf{A}^{\infty}$ the infinite frequency added inertia matrix, and $\ddot{\mathbf{x}}$ the acceleration vector. The right-hand side term will be explicited in the next paragraphs. It consists in the summation of the instantaneous hydrostatic forces $\mathbf{f^h}$, the hydrodynamic excitation forces $\mathbf{f^e}$, the wave radiation forces $\mathbf{f^r}$, the viscous hydrodynamic forces $\mathbf{f^v}$, the aerodynamic forces $\mathbf{f^a}$, the rotor gyroscopic forces $\mathbf{f^g}$, and the mooring restoring forces $\mathbf{f^m}$. This equation allows to calculate $\ddot{\mathbf{x}}$ at each time step, then the time domain motion history is obtained by double numerical integration of the acceleration vector.

2.2. Hydrostatic forces

The hydrostatic force is computed using the conventional seakeeping linearisation:

$$\mathbf{f^h}(t) = -\mathbf{K^h}\,\mathbf{x}(t). \tag{2}$$

By assigning a seawater density ρ and calculating the waterplane area A_w, the third diagonal hydrostatic stiffness coefficient is obtained as $K_{33}^h = \rho g A_w$. By denoting the displacement Δ and the transverse and longitudinal metacentric heights over the CoG respectively $\overline{GM}_T$ and $\overline{GM}_L$, the roll and pitch hydrostatic stiffness coefficients are written as $K_{44}^h = \Delta\overline{GM}_T$ and $K_{55}^h = \Delta\overline{GM}_L$. The remaining entries of the $\mathbf{K^h}$ matrix are nil for the type of structure studied.

2.3. Hydrodynamic forces

As it is frequently done in floating structure dynamic modelling, hydrodynamic forces are calculated via a superposition of inertial and viscous forces. The former are computed by NEMOH, an open source linear diffraction and radiation solver developed by the Ecole Centrale de Nantes [37], and imported within CALHYPSO in the form of a frequency-domain hydrodynamic base. This is used in turn to recreate, in the time domain, the incident wave excitation vector $\mathbf{f^e}$ and the reactive force associated to wave radiation $\mathbf{f^r}$ in the form reported next.

The jth element of the wave excitation vector is defined for an N-component, bi-dimensional wave train of incidence θ as

$$f_j^e(t) = \sum_{n=1}^{N} D_{j,n} a_n \cos\big(-\omega_n t + k_n \overline{x}(t)\cos\theta + \\ + k_n \overline{y}(t)\sin\theta + \Phi_{j,n} + \phi_n\big) \tag{3}$$

where $D_{j,n}$ and $\Phi_{j,n}$ are the amplitude and phase of the nth excitation harmonic in the jth DoF, a_n the amplitude of the corresponding spectral component (or simply the incident wave amplitude if $N = 1$), ω_n and k_n the wave component's frequency and number, ($\overline{x}$, $\overline{y}$) the structure's mean horizontal offset, and ϕ_n a randomly generated phase ($\phi_n = 0$ if $N = 1$).

The radiation force vector $\mathbf{f^r}$ is included using the linear impulsive model by Ref. [38] via the convolution integral

$$\mathbf{f^r}(t) = -\int_{t-T}^{t} \mathbf{K}(t-\tau)\dot{\mathbf{x}}(\tau)\mathrm{d}\tau, \tag{4}$$

where T is the convolution window length and $\mathbf{K}$ the convolution kernel, which is derived from the frequency/dependent radiation damping matrix [39].

Viscous forces are computed by discretising the hull into segments and evaluating the quadratic drag force acting on each wetted element applying the Morison formulation [40], proportionally to the projected area of these elements. The axial and transverse components of the local relative velocity are derived from the incident wave kinematics and the structure's motion. The adoption of axial and transverse drag coefficients — dependent on element geometry — allows to calculate the corresponding components of the drag force. The transverse drag coefficients for all cylindrical sections are assigned based on a (KC, β) pairing representative of an average regime, using the experimental data provided by Ref. [41]. The axial drag coefficients for the heave plates are adopted from Ref. [42], where such values are calibrated for thick water entrapment plates based on basin tests. The elementary drag forces are integrated over the hull to form the viscous force vector $\mathbf{f^v}$ at every time step.

2.4. Aerodynamic forces

The aerodynamic forces acting on the rotor and the tower are both assimilated to a thrust-type force, applied punctually at the rotor's and tower's respective centres of thrust. The aerodynamic torque exerted on the rotor is also computed. Given an operating condition characterised by a thrust coefficient c_T and a torque coefficient c_Q, the thrust and torque on the rotor are computed using a modified version of the coupled formulation used by Ref. [43]:

$$T = \frac{1}{2}c_T \rho_a A |U - u|(U - u)\cos\alpha, \tag{5}$$

$$Q = \frac{1}{2}c_Q \rho_a AR |U - u|(U - u)\cos\alpha, \tag{6}$$

where ρ_a denotes the air density, A the rotor swept area, R the rotor radius, U the incident wind speed at hub height, u the component of
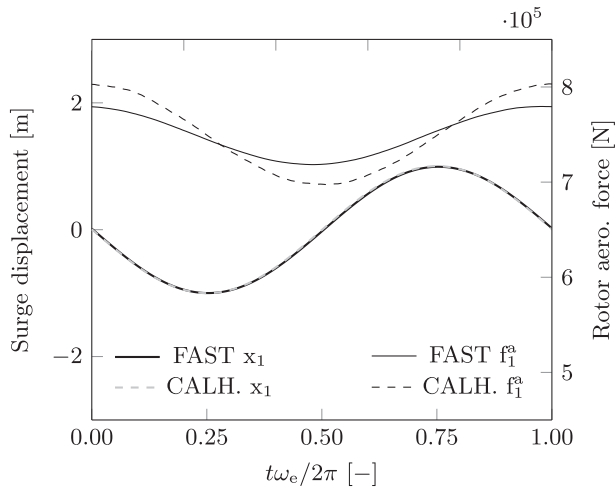
Fig. 2. Forced oscillation in the direction of wind of an operating NREL 5 MW rotor, for an excitation frequency of $\omega_e = 0.40$ rad/s.

the hub velocity in line with the incident wind speed, and α the instantaneous leeward inclination of the rotor due to platform motions. This coefficient-based reactive model assumes that blade pitch does not adjust to the aerodynamic fluctuations due to the motions of the FWT. This corresponds to an idealised implementation of a known control option for floating HAWTs where the frequency of the controller is deliberately moved below that of FWT motions, in order to avoid the appearance of negative damping [44]. The thrust T is applied horizontally in the direction of the incident wind and its moments are calculated with respect to the EoM reference point using the updated position of the hub. Q is also applied as a horizontal torque vector in the wind direction (it is assumed that the rotor is perfectly yawed into the wind at all times).

The use of a coefficient-based model ensures that the rotor's aerodynamic excitation tensor matches a prescribed (equilibrium) operating point, based on the specifications supplied by the turbine designer. However, apart from the averaging of rotor forces and the absence of the effects of turbine control, an important limitation of such models is the absence of a feedback mechanism relating the inflow speed to the fluctuations of T and Q. This causes an overestimation of the aerodynamic forces' variance in presence of windward/leeward motion which is particularly significant at low frequency, when the inflow has sufficient time to react. An example is given in Fig. 2, where the thrust component in the x direction for a rigid NREL 5 MW rotor oscillating in the direction of the incident wind is shown as predicted by FAST[1] and by the present simplified model.

The incident wind speed and operating parameters of the turbine are set at the rated point and a constant wind profile is used. The Figure shows how the coefficient-based model provides the correct average thrust and a good approximation of the shape and phasing of its evolution over time, but produces a significantly larger variance than the more sophisticated blade element momentum theory.

Finally, the thrust exerted on the tower is also computed with Equation (5), using $c_T = c_D$, the drag coefficient for a cylindrical section. In this case A denotes the tower's projected area and u the

---

[1] FAST v.8.08, using dynamic inflow. The rotor speed and blade pitch are fixed. Surge motion is obtained with the application of a harmonic horizontal force as proposed in Ref. [45].

component of the motion-induced velocity of the centre of thrust in the direction of the incident wind. The set of generalised aerodynamic forces resulting from the above model are summed and included in the term denoted $\mathbf{f^a}$.

2.5. Rotor gyroscopic forces

Past studies revealed the importance of gyroscopic coupling in floating wind dynamics [46,47]. An oscillating structure bearing a rotor revolving at constant speed receives a gyroscopic reaction moment $\mathbf{M^g}$ that can be written using the d'Alembert principle [48],

$$\mathbf{M^g}(t) = -I_r \Omega \mathbf{\Gamma}(t) \times \mathbf{i^r}(t). \tag{7}$$

In the above equation I_r represents the axial inertia of the rotor, Ω its rotational speed and $\mathbf{i^r}$ the associated unit vector, whilst $\mathbf{\Gamma} = (\dot{x}_4, \dot{x}_5, \dot{x}_6)$ denotes the structure's rotational speed vector. The gyroscopic term included in Equation (1) is then written as

$$\mathbf{f^g} = \left(0, 0, 0, M_1^g, M_2^g, M_3^g\right). \tag{8}$$

2.6. Mooring forces

CALHYPSO includes the capability for a multi-segment, quasi-static representation of catenary moorings and their forces [a similar model is described in Ref. [49]. In the present study mooring restoring forces are represented with a linearised model employing the stiffness matrix $\mathbf{K^m}$,

$$\mathbf{f^m}(t) = -\mathbf{K^m}\mathbf{x}(t), \tag{9}$$

in order not to incur in offset-dependent mooring stiffness nonlinearity and response bifurcation.

2.7. Treatment of mean inclination

The approach adopted here to treat the FWT's relatively large wind-induced inclinations is based on re/linearising the dynamic system about the tilted and offset configuration assumed by the FWT under pure wind loading. It is assumed that further dynamic oscillations of small amplitude will occur around this position.

A preliminary computation is required to obtain said offset configuration: in this study this consists in applying the rotor forces obtained with the desired operational regime and running the dynamic simulation in the absence of incident waves until the steady-state, static offset is attained. Small static rotations are found about the z axis (around 0.2°) and about the horizontal axis aligned with the wind (around 0.4°). These are respectively due to the eccentricity of the thrust force with respect to the z axis and the stator's reaction to the rotor torque. These secondary rotational components are neglected whilst the larger leeward equilibrium angle due to wind overturning is used to rewrite the EoM terms with the methods explained next.

As it will be pointed out in Section 4, because of the non-linearities present in the model the effective mean inclinations in the wind-and-wave dynamic simulations do slightly depart from the static values obtained as described above. Although this problem may be solved iteratively, in the present study this relatively small discrepancy between input and output mean inclination is accepted.

Rigid body inertia. The generalised inertia matrix is actualised to the mean rotated position using

$$\mathbf{M} = \begin{pmatrix} m & 0 & 0 & 0 & mz_C & -my_C \\ & m & 0 & -mz_C & 0 & mx_C \\ & & m & my_C & -mx_C & 0 \\ & & & J_{11} & I_{12} - mx_C y_C & I_{13} - mx_C z_C \\ & \text{sym.} & & & J_{22} & I_{23} - my_C z_C \\ & & & & & J_{33} \end{pmatrix},$$

(10)

$$J_{11} = I_{11} + m\left(y_C^2 + z_C^2\right),$$
$$J_{22} = I_{22} + m\left(x_C^2 + z_C^2\right),$$
$$J_{33} = I_{33} + m\left(x_C^2 + y_C^2\right),$$

(11)

where the terms denoted I are the elements of the central inertia tensor. Vector (x_C, y_C, z_C) represents here the position of the centre of mass in the inertial SoR after applying the rotation.

Hydrostatics. A set of preliminary calculations determined that the changes in hydrostatic stiffness never exceed 1% for the treated hull and its mean inclinations. For vertical hydrostatic stiffness they consist in computing the updated waterplane area, whilst for the rotational terms the positions of G (centre of gravity), B (centre of hull volume), and M (longitudinal/transversal metacentre) are recalculated after applying an isocarenic inclination. Thus their heights over the reference keel point K concur to determining the updated hydrostatic restoring moment arm $\overline{GM} = \overline{KB} + \overline{BM} - \overline{KG}$ and finally the stiffness terms K_{44}^h and K_{55}^h as described in 2.2. Following these considerations, it was decided to neglect the nonlinear hydrostatic effects due to the mean inclination, (which is in the order of 6° in the presented case study). For what concerns the rotational terms, the above finding is consistent with the well-known behaviour of wall-sided floating bodies, which exhibit linear hydrostatic restoring up to trim/heel angles of about 10° [see for instance [50]. Thanks to the choice of point O at the SWL, no extra-diagonal terms appear within the $\mathbf{K}^h$ matrix following a static inclination.

Potential flow hydrodynamics. The geometric nonlinearity affecting the hull's wave diffraction and radiation in presence of a significant inclination can be treated by updating the hydrodynamic mesh to the new mean position, effectively re-linearising inertial hydrodynamic forces about a new equilibrium point. Fig. 3 shows the upright hydrodynamic mesh and the actualised meshes following application of wind overturning in the x and y direction. Slender cross-beams are omitted from the potential flow hydrodynamic mesh for computational efficiency reasons. It can be noticed that in the presence of a rotation about the x axis the xz planar symmetry is lost, leading to the need to discretise the entire wetted surface. An important remark based on this figure is that the water entrapment plates undergo significant vertical excursion in (b) and (c), causing the potential flow hydrodynamic regime perturbations already scrutinised in Ref. [34]. Their impact on FWT dynamic response in the time domain will be treated in Section 4.

Viscous hydrodynamics. The process of calculating the hydrodynamic drag forces includes updating the position of the discrete hull elements at every time step as a consequence of the motion of the structure. Thus the preliminary computation of the mean inclination described above needs not be an input, since the correct drag element displacements are continuously applied in the time domain. This implies that the drag elements are exposed to wave particle kinematics of varying intensity depending on their vertical excursion and of varying phasing depending on their horizontal excursion. Fig. 4 provides a visual example of the lateral drag force exerted on a platform column undergoing excursion.
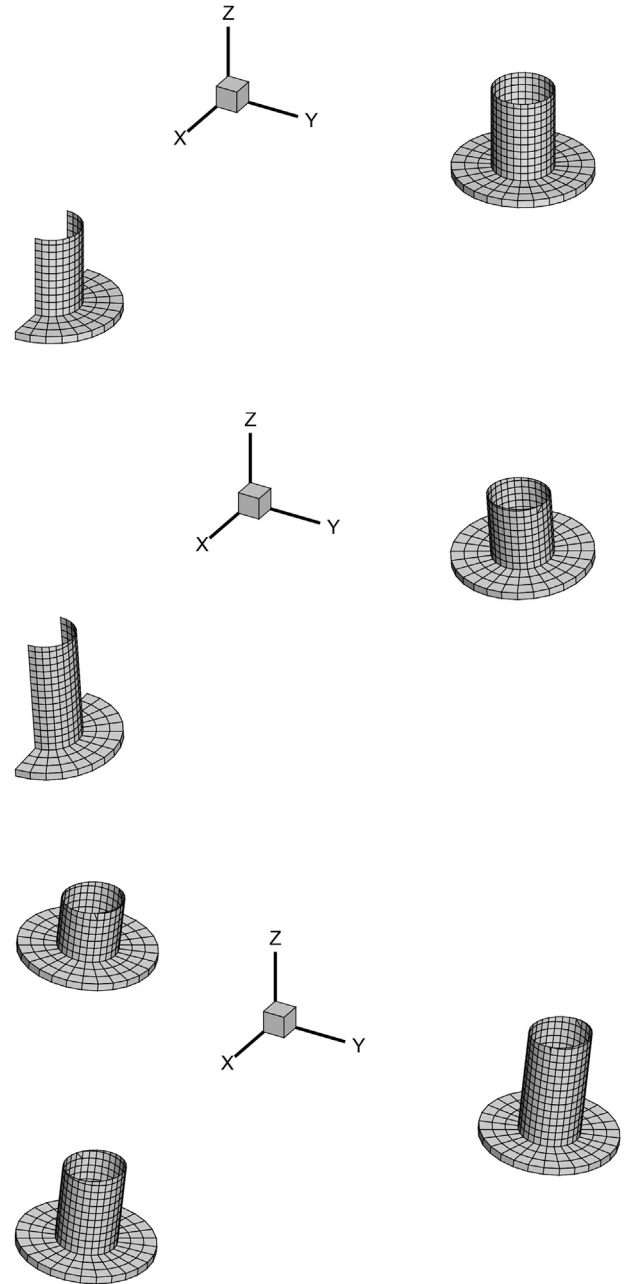

Fig. 3. Wetted surface discretisations used for the wave diffraction and radiation calculations. Above: upright. Centre: with rotation about y. Below: with rotation about x.

Mooring forces. All nonlinearities related to the catenary mooring system are neglected to keep the focus on platform hydrodynamics, hence the initial linearised stiffness matrix $\mathbf{K}^m$ is employed unchanged.

3. Definition of case study

To keep the focus sharp, this study adopts the modfied Dutch Tri-floater, a FWT concept elaborated by Ref. [51] and modified by Ref. [34], which is particularly suited to show the effects of wind-induced inclination on coupled dynamic response. This structure is subjected to inline and cross wind and wave regimes using a homogeneous wind profile and regular or irregular waves as inputs.
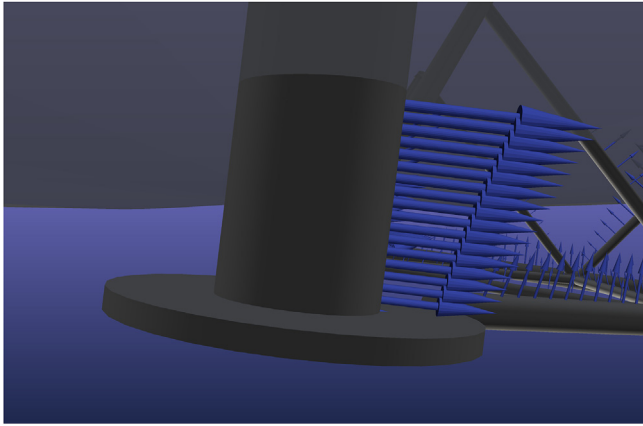
Fig. 4. Snapshot of transverse drag forces exerted on a platform column under a 12 s wave of 4 m height. The arrow size is proportional to the magnitude of the local force.

In the irregular wave cases, the standard JONSWAP formulation is used to calculate the input spectrum, employing $\gamma = 3.3$. All wavetrains propagate in the positive x direction, exciting the structure in presence of zero, inline, and cross wind at rated speed, constant over time. The wind turbine's operating conditions are parked for zero wind speed and rated for the cases including wind. A compact definition of the loading cases considered is supplied in Table 1.

The three-column semi-submersible floating platform is coupled to a NREL 5 MW reference offshore wind turbine [52], totalling 3124 t of displacement (Fig. 5).

Station keeping is assured by a conventional chain-wire hybrid, 6-point mooring system (line properties are given in Table 2) with two lines departing from the outer bottom of each column, at a radial distance of 4.0 m from the centre of the column. A water depth of 50 m is assumed.

The parameters defining the platform are given in Table 3, whilst the turbine is detailed in Table 4.

As said the mooring restoring forces are included with a simple restoring term; the undisturbed mooring weight, equating 183.5 t, is accounted as a lump mass at fairlead height within the weight computation. Equation (12) defines the values assigned to the mooring stiffness tensor, as calculated by Ref. [51]. The units used are [m, rad] for displacements and [N, Nm] for the generalised forces.
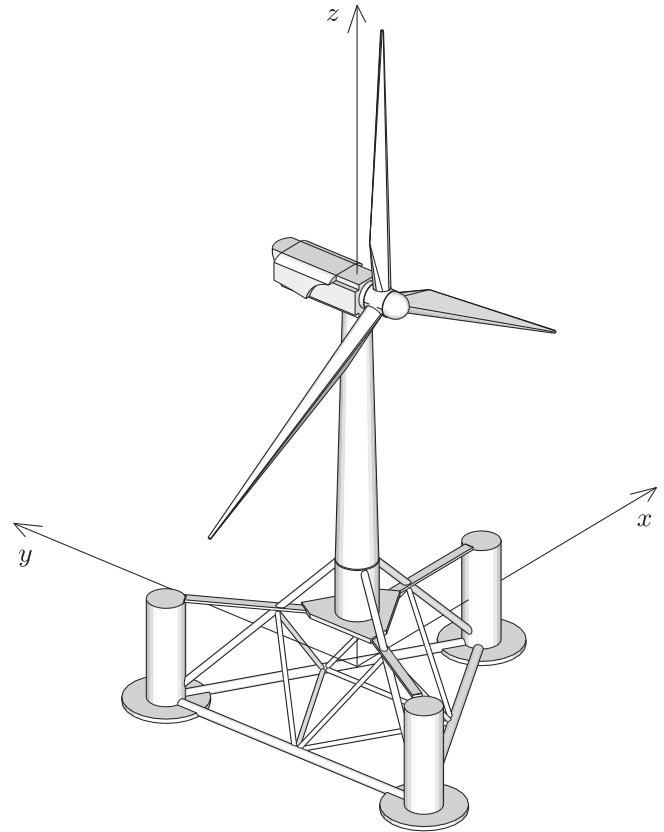

Fig. 5. Modified Dutch Tri-floater with 5 MW class horizontal axis wind turbine. The latter is adapted from a graphical model made available by Ref. [53].

Table 2
Properties of a Dutch Tri-floater mooring line.

Component	Studless chain	Wire
Material	Steel	Steel
Nominal diameter [m]	0.15	0.16
Unstretched length [m]	190	225

Table 1
Definition of loading cases. Angles are measured in the horizontal plane counter-clockwise starting from the x axis (90° is aligned with y).

Regular waves			
Loading case name	LC0	LCX	LCY
Wind speed [m/s]	0.0	11.4	11.4
Wind direction [deg]	–	0.0	90.0
Turbine operation	Parked	Rated	Rated
Wave height [m]	4.0	4.0	4.0
Wave direction [deg]	0.0	0.0	0.0
Irregular waves			
Loading case name	LC0i	LCXi	LCYi
Wind speed [m/s]	0.0	11.4	11.4
Wind direction [deg]	–	0.0	90.0
Turbine operation	Parked	Rated	Rated
Sig. wave height [m]	4.0	4.0	4.0
Peak period [s]	10.0	10.0	10.0
Wave direction [deg]	0.0	0.0	0.0

Table 3
Modified Dutch Tri-floater parameters. Mass and inertia quantities are expressed with respect to the origin O at SWL.

Geometry	
Design draft [m]	12.0
Hull volume at design draft [m^3]	3048
Column centre-to-centre spacing [m]	68.0
Column diameter [m]	8.0
Column depth incl. plate [m]	24.0
Plate diameter [m]	18.0
Plate thickness [m]	1.0
Bracing diameter [m]	1.0–2.0
Mass & inertia	
Mass [t]	2263
Vertical position of CoG [m]	−0.1
Roll/pitch moment of inertia [tm^2]	$1.535 \cdot 10^6$
Yaw moment of inertia [tm^2]	$2.522 \cdot 10^6$

Table 4

Adapted 3-blade upwind 5 MW NREL offshore wind turbine data. Mechanical quantities are expressed with respect to the origin O at SWL with the exception of the rotor's inertia.

Mechanical parameters	
Overall mass [t]	678
Overall vertical position of CoG [m]	83.0
Overall roll/pitch moment of inertia [tm^2]	$3.779 \cdot 10^6$
Overall yaw moment of inertia [tm^2]	$5.220 \cdot 10^3$
Rotor axial inertia [tm^2]	$3.876 \cdot 10^4$
Elevation of tower/platform interface [m]	25.0
Rotor diameter [m]	126
Hub height [m]	90.0
Rated operating parameters	
Incident wind speed [m/s]	11.4
Rotor speed [rpm]	12.1
Rotor thrust coefficient c_T [−]	0.82
Rotor torque coefficient c_Q [−]	0.066
Tower drag coefficient c_D [−]	1.0

$$\mathbf{K^m} = \begin{pmatrix} 1.6 \cdot 10^5 & 0 & 0 & 0 & 1.9 \cdot 10^6 & 0 \\ & 1.6 \cdot 10^5 & 0 & -1.9 \cdot 10^6 & 0 & 0 \\ & & 1.5 \cdot 10^5 & 0 & 0 & 0 \\ & & & 1.1 \cdot 10^8 & 0 & 0 \\ & \text{sym.} & & & 1.1 \cdot 10^8 & 0 \\ & & & & & 1.7 \cdot 10^8 \end{pmatrix} \tag{12}$$

4. Results

This section presents the results of the set of simulations defined above. The preliminary offset calculation yields the generalised position vectors

$$\text{LCX \& LCXi}: \ \mathbf{x} = \begin{pmatrix} 3.96 & 0.08 & 0.00 & 0.41 & 6.37 & 0.18 \end{pmatrix}^T$$

$$\text{LCY \& LCYi}: \ \mathbf{x} = \begin{pmatrix} -0.08 & 3.96 & 0.00 & -6.37 & 0.41 & 0.18 \end{pmatrix}^T \tag{13}$$

(a) Surge. $\omega_n \approx 0.18$ rad/s.

(b) Sway. $\omega_n \approx 0.18$ rad/s.

(c) Heave. $\omega_n \approx 0.46$ rad/s.

(d) Roll. $\omega_n \approx 0.25$ rad/s.

(e) Pitch. $\omega_n \approx 0.25$ rad/s.

(f) Yaw. $\omega_n \approx 0.18$ rad/s.

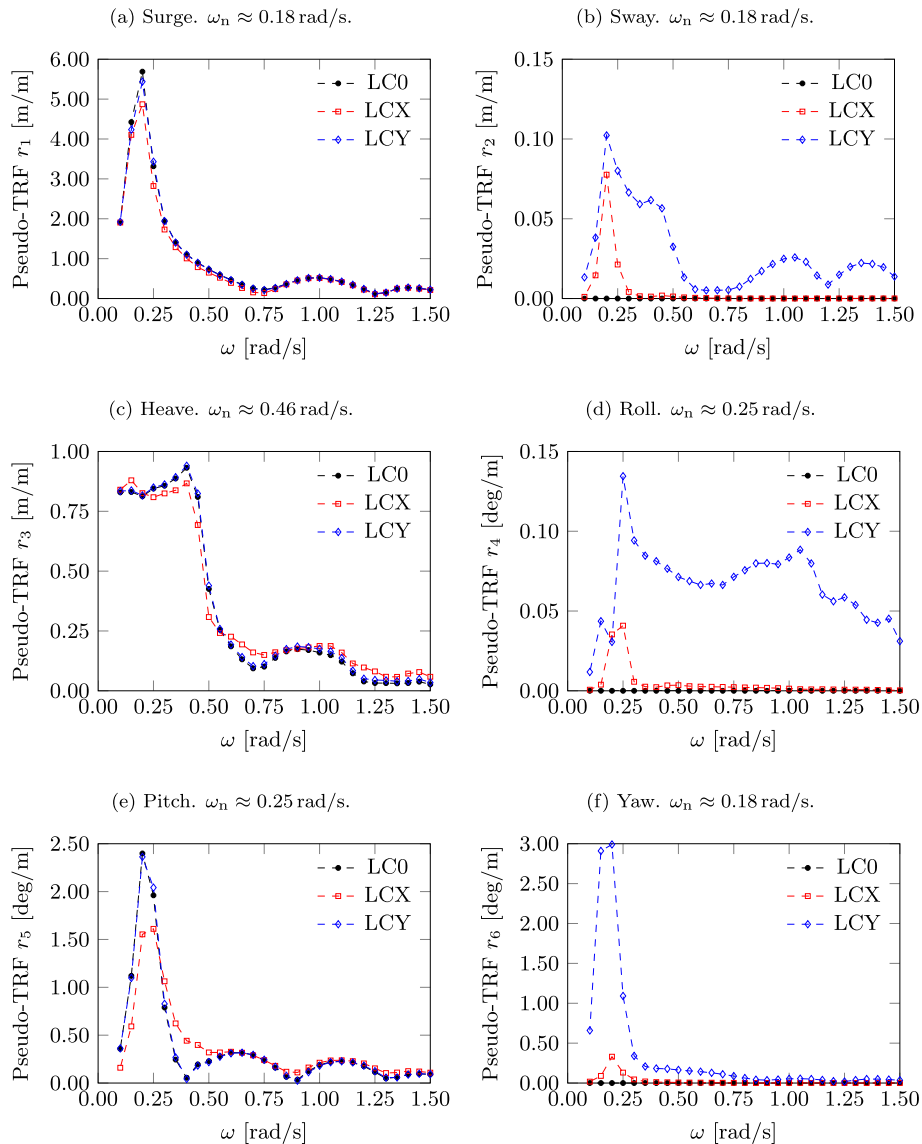**Fig. 6.** Pseudo-transfer functions of a modified Dutch Tri-floater subjected to wind and regular wave excitation.

(a) Surge.

(b) Sway.
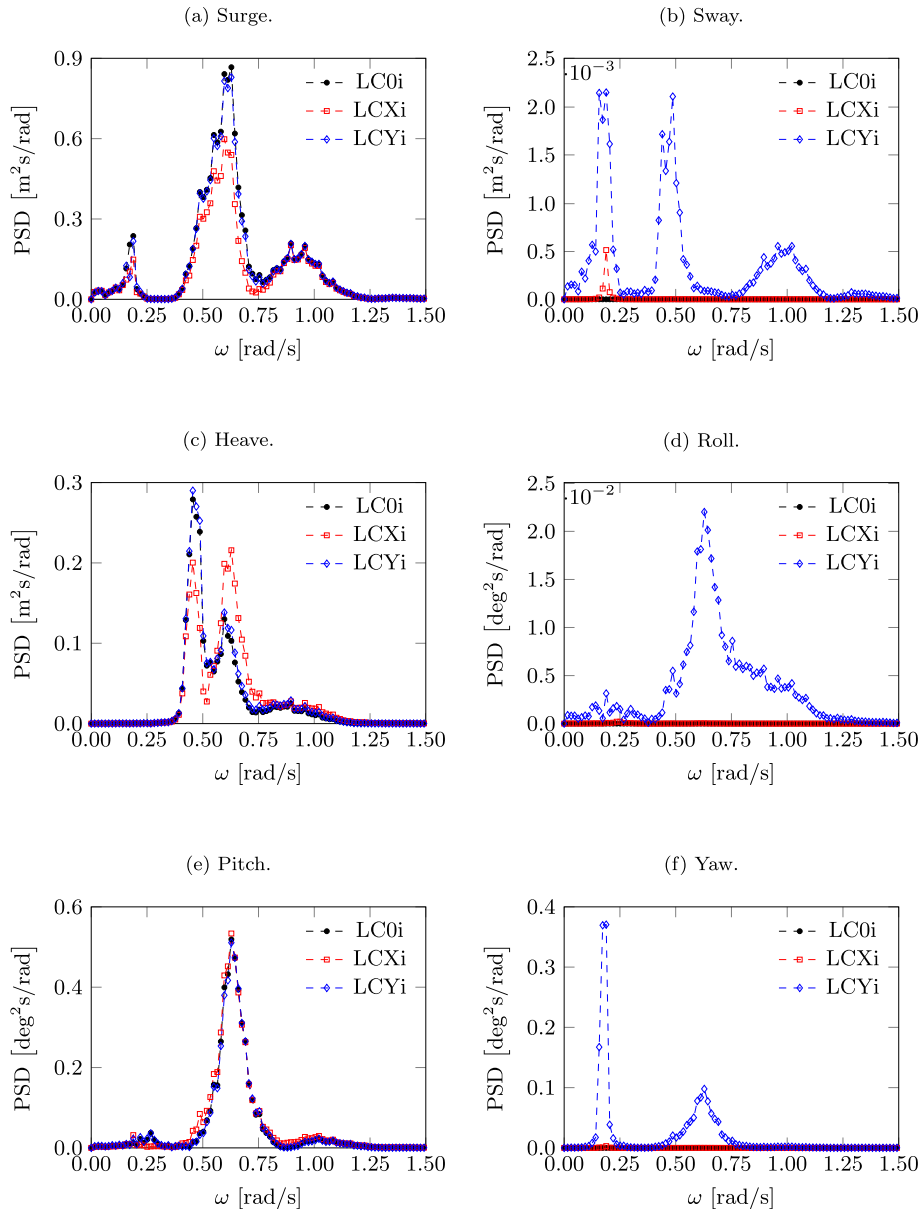
(c) Heave.

(d) Roll.

(e) Pitch.

(f) Yaw.

Fig. 7. Power spectral density of the motions of a modified Dutch Tri-floater subjected to wind and irregular wave excitation.
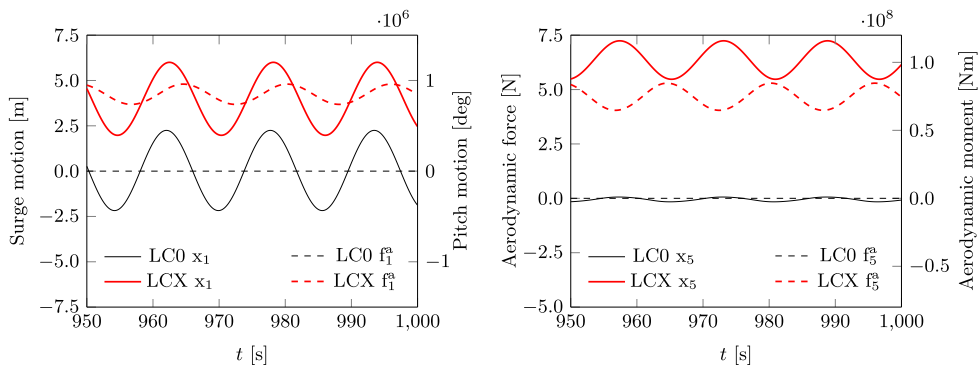
Fig. 8. Time-domain output motion and aerodynamic forcing in surge (left) and pitch (right), for an incident wave of 0.40 rad/s.
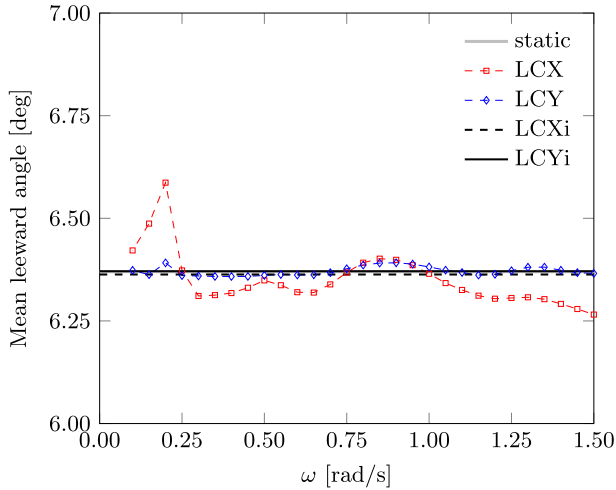
Fig. 9. Mean leeward angles obtained from wind-and-wave dynamic simulations.

with displacements given in [m] and rotations in [deg]. As one may expect, the most significant static offsets are a displacement in the wind direction, which is resisted by the mooring system, and a leeward rotation mainly countered by hydrostatic restoring. The symmetric stiffness features of the system also emerge from Equation (13). The FWT's dynamic response in regular waves exhibits nearly harmonic form at steady state. Obtaining the pseudo-transfer function of motion in any DoF i requires post-treating the time-domain signal, which in this case is done by

$$r_i(\omega) = \frac{\max[x_i(t,\omega)] - \min[x_i(t,\omega)]}{H}, \tag{14}$$

where $H = 2a$ is the incident wave height. It must be pointed out that because of the nonlinearities present in the model, the pseudo-transfer function magnitude is dependent on the excitation magnitude within certain bands. In case wind forces are applied, the response characteristics r_i are to be interpreted as the normalised amplitude of the dynamic response to wave excitation about the mean wind-induced offset.

Fig. 6 displays the ensemble of the pseudo-transfer functions calculated for the loading cases defined in Table 1. For each DoF the corresponding uncoupled, undamped natural frequency ω_n is reported to facilitate interpretation. It can be seen that the most important response features lie in the xz plane (surge, heave, pitch), which is expected for a 2D wave train propagating in the x direction over a roughly symmetric structure. Most resonances are confined

at the far left of the studied band, a desirable hydromechanic feature in light of the distribution of wave energy and the subsequent first order excitation. An in-depth screening of these results is given in Section 5.

Fig. 8 provides a snapshot of a dynamic simulation in regular waves after the steady state is reached. The quasi-harmonic motion time histories of surge and pitch are shown with their respective aerodynamic excitation signals, for an incident wave frequency of 0.40 rad/s and two different loading cases. The mean forces and by consequence the offsets obtained when wind is applied are immediately evident. This case will be later used for clarification of the inter-DoF aerodynamic coupling observed around said frequency.

The motion outputs of the irregular wave simulations are shown in Fig. 7 in spectral form. The underpinning time series have a duration of 2 h and represent the fully developed dynamic response of the structure in a stationary sea state. The input spectral realisation − defined by a particular choice of component phases − is the same for all loading cases. These results will be used in Section 5 to contextualise the dynamic response features of the system for a specified, realistic met-ocean condition: the fact that most of the input wave energy lies between 0.5 and 0.9 rad/s brings out the response features of the studied FWT in this central band.

Finally, the mean leeward inclination angles attained in the steady-state phase of all dynamic simulations are plotted (in absolute value) in Fig. 9. It appears that although limited in magnitude, discrepancies exist between the assumed mean inclination and that effectively produced by the dynamic simulations in regular waves. This is especially pronounced for load case LCX, where nonlinear forces with non-zero mean are present (i.e. hydrodynamic drag) which have a large component in the same plane of the leeward inclination. The subsequent deviations from the statically calculated inclination do not exceed 4% and are deemed tolerable.

5. Discussion

Numerous elements of interest can be derived from the results shown in Section 4. They will be discussed in the following by looking at a DoF at a time, then the key findings will be related to existing experimental results.

5.1. Dynamic response analysis

Response in **surge** (Fig. 6a) is not particularly affected by the presence of rotor forces and platform inclinations. Only when the rotor is aligned with the surge motion (LCX) a minor dampening effect occurs due to aerodynamic damping thereby reducing the
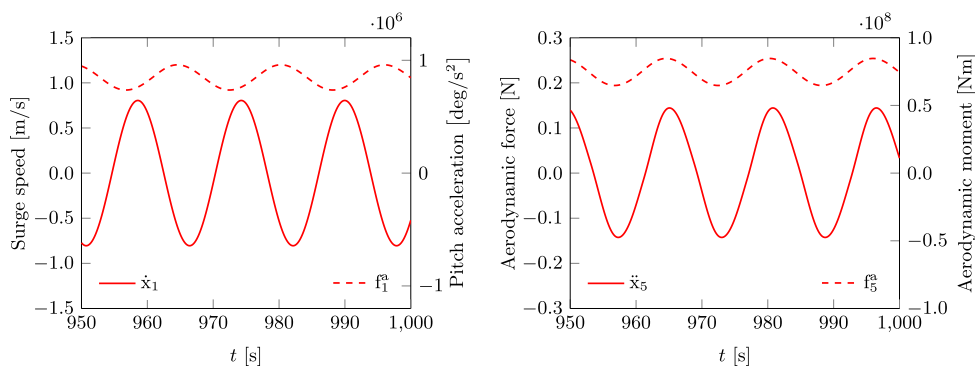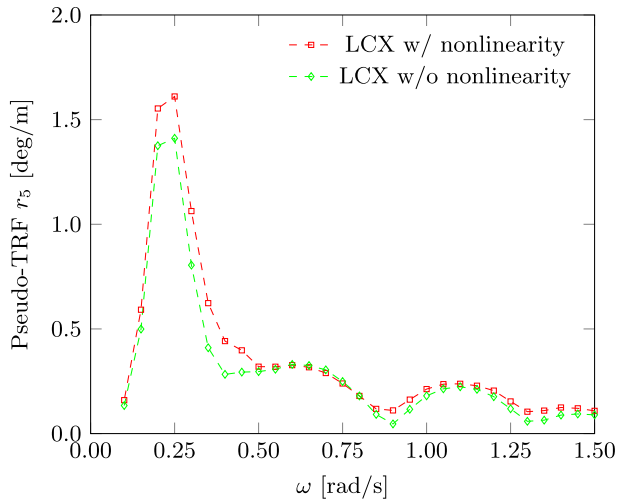

Fig. 10. Time-domain surge speed (left) and pitch acceleration (right) of loading case LCX, for an incident wave of 0.40 rad/s. The respective aerodynamic force and moment signals are also shown.

Fig. 11. Pitch response characteristic predicted with and without treatment of the geometric nonlinearity.

amplitude of the oscillation at the peak, located at 0.18 rad/s. The reduction in off-peak response is instead related to the alteration of inertial hydrodynamic excitation of the surge-pitch coupled mode. Observing Fig. 7a reveals the significance of these features in irregular waves.

As expected, and visible from Figs. 6b and 7b, **sway** response is identically zero when the structure receives wave excitation only (directed along the *x* axis). Resonant inter-DoF coupling and loss of hydrodynamic *xOz* symmetry respectively cause small sway response for collinear and cross-wind loading cases.

Heave motion (Fig. 6c) exhibits a marked dependence on rotor forces and inclinations in the case of collinear wind and waves: excitation suppression around $\omega \approx 0.7$ rad/s becomes less pronounced mainly because of the simultaneous vertical excursion of two heave plates toward the free surface (see Fig. 3, centre). This in turn triggers.

(1) an increase (and a phase shift) of the inertial wave excitation, an effect already discussed by Ref. [34], and secondly
(2) an increase in hydrodynamic drag under the action of stronger wave kinematics.

Whilst effect (2) significantly contributes to altering response in said central band, effect (1) is solely at the root of the increased response observed at higher frequencies. The slight reduction of motion amplitude observable around the resonance peak is also an effect of the large inclination due to heave-pitch coupling deriving from imbalance in wave radiation forces (in the model: significant extra-diagonal terms appear in the added mass tensor). The prevalence of these effects in the central band makes them significant in the studied irregular wave scenario, as observable from Fig. 7c.

Roll (Fig. 6d) is another DoF whose response is nil in the upright position and in the absence of rotor forces. Whilst the results are practically unchanged for LCX apart from a small resonance effect, a broad, albeit limited motion response is present in cross-wind conditions because of the loss of symmetry in port-starboard column excitation (see Fig. 3, below), which is also detectable in Fig. 7d.

Fig. 6e reveals that **pitch** response at low frequency is particularly affected by the action of wind forces and the subsequent inclination in the collinear case. As expected, the resonance peak around $\omega_n = 0.25$ rad/s is attenuated by the aerodynamic damping, whose impact is otherwise insignificant in the cross-wind case. The increased response manifested by LCX at the far right of the peak is exclusively due to the plate excursion effect (1) described above. A most prominent feature of pitch motion for the collinear loading case is the appearance of significant response in the immediate vicinity of the resonance peak, where wave excitation is suppressed for LC0 and LCY. This is caused by two concurring factors: heave plate excursion effect (1) and the aerodynamic excitation of pitch caused by surge motion. This aerodynamically sourced, inter-DoF coupling will be further clarified in 5.2. In the studied irregular wave case, these pitch response features lose significance due to the low energy available below 0.5 rad/s (Fig. 7e).

Figs. 6f and 7f display the response in **yaw**, which rests unexcited by the waves in the absence of wind. The combination of gyroscopic coupling and resonance produces a limited response peak for LCX. It is the cross wind-and-wave cases LCY and LCYi that display the largest motion: the immersion of the port column and the emersion of the starboard column (Fig. 3, below) cause an imbalance creating the potential for broad yaw forcing across the studied frequency band. Where this excites resonant motion, in the band around 0.18 rad/s, the dynamic response becomes very significant. It should be remarked that since the present model omits the damping contributions of mooring line drag and rotor yawing, peak yaw response is likely overestimated.

5.2. Aerodynamic inter-DoF coupling

For the presently studied FWT, the frequency band between 0.25 rad/s and 0.55 rad/s is rich in inter-DoF coupling phenomena, which intertwine with the effects of wind-induced inclination in a complex fashion. As pointed out in 5.1, aerodynamically sourced surge-pitch coupling explains in part the observed difference in response between LCX and the other regular wave loading cases (cf. Fig. 6e). LCX is the sole case where the rotor is operating in line with the hub speeds induced by pitch motion. Reactive aerodynamic damping is a well-known consequence of this set-up. Within the frequency band centred on 0.4 rad/s, however, wave-induced pitch motion is relatively small and the aerodynamic force oscillations due to the motion-induced hub velocity tend to be more associated with surge response. This is made evident by rearranging the LCX results of Fig. 8 (left) in terms of surge speed and aerodynamic force, as displayed in Fig. 10 (left). Hence it emerges the relationship between surge and the aerodynamic force in the *x* direction: such force appears to react to surge motion since it is in near phase opposition with surge velocity. At the same time, its fluctuations are transferred as variations of external pitch moment to the FWT assembly. The phasing between aerodynamic excitation and pitch acceleration visible in Fig. 10 (right) for case LCX reflects this inter-

Table 5
Summary of the observed wind-induced inclination effects on FWT dynamics.

Inclination effect	Nature of force	Location	Affected DoF	Bandwidth	LC type
Plate excursion	Hydro. inertial	Heave plates	Heave, pitch	Wide	Collinear
	Hydro. viscous	Heave plates	Heave	Narrow	Collinear
	Hydro. inertial	Heave plates	Roll	Wide	Cross
Column excursion	Hydro. inertial	Columns	Yaw	Wide	Cross

DoF coupling effect, as the aerodynamic reactions are driving, not dampening, pitch motion. Of course, the retroactions present in the dynamic system close the loop and ultimately render the one-way cause-and-effect dynamic explained above less clear-cut. The effect of the rotor control strategy — conventional, low-frequency [44], or with active motion damping [54] — on the intensity of this coupling is likely significant, although not treated here. It should also be pointed out that since the present thrust-based model tends to overestimate the aerodynamic reactive force (see Fig. 2), the strength of this coupling mechanism is likely overestimated as well, at least in the absence of active motion damping by control.

5.3. Experimental evidence of heave plate excursion effect

The observed interaction between heave plates and wave forces in presence of large vertical excursions is only accounted for by nonlinear fluid dynamic models or, to a certain extent, by re-linearising a linear model about the offset position as done here, thereby limiting the errors caused by geometric nonlinearity. A past publication by Ref. [14] shows that the experimentally observed dynamics of a similar FWT subjected to collinear wind and waves are not entirely captured using the conventional modelling method based on linearising the fluid-structure interaction about the initial equilibrium. Virtually equivalent results are also available in Refs. [51,55]. The predictions of pitch — a key DoF for FWTs — shown by these authors are particularly inaccurate in the 0.25—0.50 rad/s band, that is around the excitation suppression point next to the resonance peak: said numerical models underestimate the relatively large pitch motion obtained experimentally. On the contrary, the modelling strategy presented in this study may enable a more accurate representation of FWT dynamics in this range, as suggested by the sustained pitch response of LCX to the right of the main peak in Fig. 6e. This can also be shown by applying the conventional linearisation of potential hydrodynamics to the above case study, which provides for instance the pitch response characteristic provided with Fig. 11. An ongoing simulation benchmark campaign is expected to verify this capability by application of the present methodology to an experimentally documented case.

6. Conclusions

The present work builds on previous findings which suggest that low-draft water entrapment plates undergoing excursion may alter the dynamics of a FWT when both wind and wave loads are present [34]. The use of a time-domain model with inclination-dependent, yet linear implementation of potential flow hydrodynamics enables to confirm these features, detected among a range of aero-hydrodynamic coupling effects. Table 5 provides a summary of the observed couplings which descend from the mean wind-induced inclinations (about 6°) attained when the turbine is operating at rated conditions. Both inline and cross wind-and-wave cases are treated, showing that the geometric nonlinearity descending from the leeward inclination of the FWT significantly affects dynamic response through the vertical excursion of the columns and the water entrapment plates. With respect to the direction of wave propagation, in-plane response (surge, heave, pitch) is mostly affected by inclination for collinear wind and waves, whilst out-of-plane response (sway, roll, yaw) is shown to be altered by the application of cross-wave wind.

Further work will be required to broaden the characterisation of the inclination effects to cover more operating conditions, different highly compliant FWT concepts (e.g. a soft spar), and possibly the interaction of these phenomena with wind turbulence and rotor control. A high-level classification of FWT concepts may also be performed, for instance by evaluating their motion sensitivity to the inclination effects as a function of governing parameters such as the wind load to displacement ratio.

Given that the cost optimisation of FWT designs may keep pushing the allowable wind-induced inclinations further, the nonlinearities inherent to the coupled dynamic system are likely to increasingly manifest, more than anything else in the highly dynamic, dimensioning loading cases. The dynamic modeller must then apply careful judgement: methodologies of increasing complexity will be required, likely departing from conventional offshore structure analysis. Although the present method can represent a computationally efficient alternative to treating geometric nonlinearity, higher-order resolution of fluid-structure interaction is likely required to accurately compute the hydrodynamic loads in presence of larger inclinations. Nonlinear angular resolution of the EoM also becomes appropriate where angles exceed magnitudes of 10—15° and the linear superposition of rotations is no longer accurate.

References

[1] EWEA, Deep Water — The Next Step for Offshore Wind Energy, Tech. rep., European Wind Energy Association, 2013.

[2] D. Roddier, C. Cermelli, A. Aubault, A. Weinstein, WindFloat: a floating foundation for offshore wind turbines, J. Renew. Sustain. Energy 2 (3) (2010) 033104, http://dx.doi.org/10.1063/1.3435339.

[3] J. Bard, HiPRWind: high-power, high-reliability wind technology, in: Proc. SET-Plan Conference 2011, Warsaw, Poland, 2011.

[4] M. Monnier, Eolien en mer | France Energie Eolienne, online:, 2015 http://fee.asso.fr/politique-de-leolien/eolien-en-mer/.

[5] Main(e) International Consulting, Floating Offshore Wind Foundations: Industry Consortia and Projects in the United States, Europe and Japan, Tech. rep., Main(e) International Consulting LLC, 2013.

[6] J.M. Jonkman, Dynamics Modeling and Loads Analysis of an Offshore Floating Wind Turbine, Tech. Rep. NREL/TP-500—41958, National Renewable Energy Laboratory Golden, CO, USA, 2007.

[7] J.M. Jonkman, FAST | NWTC Information Portal, online:, 2015 https://nwtc.nrel.gov/FAST.

[8] M. Karimirad, Modeling aspects of a floating wind turbine for coupled wave—wind-induced dynamic analyses, Renew. Energy 53 (2013) 299—305, http://dx.doi.org/10.1016/j.renene.2012.12.006.

[9] DTU Wind Energy, Welcome to HAWC2, online:, 2015 http://www.hawc2.dk/.

[10] M. Collu, M. Borg, A. Shires, F.N. Rizzo, E. Lupi, FloVAWT: further progresses on the development of a coupled model of dynamics for floating offshore VAWTs, in: Proc. 33rd International Conference on Ocean, Offshore and Arctic Engineering, San Francisco, CA, USA, 2014.

[11] K. Wang, C. Luan, T. Moan, M.O.L. Hansen, Comparative study of a FVAWT and a FHAWT with a semi-submersible floater, in: Proc. 24th International Ocean and Polar Engineering Conference, Busan, Korea, 2014.

[12] A.J. Coulling, A.J. Goupee, A.N. Robertson, J.M. Jonkman, H.J. Dagher, Validation of a FAST semi-submersible floating wind turbine numerical model with DeepCwind test data, J. Renew. Sustain. Energy 5 (2) (2013) 023116, http://dx.doi.org/10.1063/1.4796197.

[13] M. Masciola, A. Robertson, J. Jonkman, A. Coulling, A. Goupee, Assessment of the importance of mooring dynamics on the global response of the DeepCwind floating semisubmersible offshore wind turbine, in: Proc. 23rd International Offshore and Polar Engineering Conference, Anchorage, AK, USA, 2013.

[14] M. Philippe, A. Courbois, A. Babarit, F. Bonnefoy, J.-M. Rousset, P. Ferrant, Comparison of simulation and tank test results of a semi-submersible floating wind turbine under wind and wave loads, in: Proc. 32nd International Conference on Ocean, Offshore and Arctic Engineering, American Society of Mechanical Engineers, Nantes, France, 2013.

[15] C.A. Cermelli, D.G. Roddier, Experimental and numerical investigation of the stabilizing effects of a water-entrapment plate on a deepwater minimal floating platform, in: Proc. 24th International Conference on Offshore Mechanics and Arctic Engineering, Halkidiki, Greece, 2005.

[16] H. Cozijn, R. Uittenbogaard, E. ter Brake, Heave, roll and pitch damping of a deepwater CALM buoy with a skirt, in: Proc. 15th Offshore and Polar Engineering Conference, Seoul, Korea, 2005.

[17] A. Aubault, C.A. Cermelli, D.G. Roddier, Structural Design of a Semi-submersible Platform with Water-entrapment Plates Based on a Time-domain Hydrodynamic Algorithm Coupled with Finite Elements, in: Proc. 16th International Offshore and Polar Engineering Conference, San Francisco, CA, USA, International Society of Offshore and Polar Engineers, 2006.

[18] online:, Products — WindFloat, 2015 http://www.principlepowerinc.com/products/windfloat.html.

[19] L. Tao, S. Cai, Heave motion suppression of a spar with a heave plate, Ocean. Eng. 31 (5) (2004) 669—692.

[20] H. Kojima, T. Ijima, A. Yoshida, Decomposition and interception of long waves by a submerged horizontal plate, in: Proc. 22nd Conference on Coastal Engineering, Delft, The Netherlands, 1990, pp. 1228—1241.

[21] X. Yu, M. Isobe, A. Watanabe, Wave breaking over submerged horizontal plate, J. Waterw. Port Coastal Ocean Eng. 121 (2) (1995) 105—113, http://dx.doi.org/10.1061/(ASCE)0733-950X(1995)121:2(105).

[22] Y. Zhao, J. Yang, Y. He, Preliminary design of a multi-column TLP foundation for a 5-MW offshore wind turbine, Energies 5 (12) (2012) 3874—3891, http://dx.doi.org/10.3390/en5103874.

[23] C.P. Butterfield, W. Musial, J. Jonkman, P. Sclavounos, L. Wayman, Engineering challenges for floating offshore wind turbines, in: Proc. Offshore Wind International Conference and Exhibition, National Renewable Energy Laboratory, Copenhagen, Denmark, 2005.

[24] J. Sweetman, Floating Offshore Wind Turbines: Conceptual Assessment of Highly Compliant Platforms Using Theory, Design and Simulation, online:, 2015 http://grantome.com/grant/NSF/CBET-1133682.

[25] M. Borg, M. Collu, F.P. Brennan, Offshore floating vertical axis wind turbines: advantages, disadvantages, and dynamics modelling state of the art, in: Proc. RINA Marine & Offshore Renewable Energy International Conference, RINA, London, UK, 2012, pp. 33—46.

[26] M. Cahay, E. Luquiau, C. Smadja, F. Silvert, Use of a vertical wind turbine in an offshore floating wind farm, in: Proc. Offshore Technology Conference 2011, Houston, TX, USA, 2011, http://dx.doi.org/10.4043/21705-MS.

[27] F. Huijs, J. Mikx, F. Savenije, E.-J. de Ridder, Integrated Design of Floater, Mooring and Control System for a Semi-submersible Floating Wind Turbine, Tech. rep., 2013.

[28] F. Huijs, R. de Bruijn, F. Savenije, Concept design verification of a semi-submersible floating wind turbine using coupled simulations, Energy Proc. 53 (2014) 2—12, http://dx.doi.org/10.1016/j.egypro.2014.07.210.

[29] M. Le Boulluec, J. Ohana, A. Martin, A. Houmard, Tank testing of a new concept of floating offshore wind turbine, in: Proc. 32nd International Conference on Ocean, Offshore and Arctic Engineering, Nantes, France, 2013.

[30] L. Wang, B. Sweetman, Simulation of large-amplitude motion of floating wind turbines using conservation of momentum, Ocean. Eng. 42 (2012) 155—164, http://dx.doi.org/10.1016/j.oceaneng.2011.12.004.

[31] B. Sweetman, L. Wang, Floating offshore wind turbine dynamics: large-angle motions in Euler-space, J. Offshore Mech. Arctic Eng. 134 (3) (2012) 031903, http://dx.doi.org/10.1115/1.4004630.

[32] L. Wang, B. Sweetman, Multibody dynamics of floating wind turbines with large-amplitude motion, Appl. Ocean Res. 43 (2013) 1—10, http://dx.doi.org/10.1016/j.apor.2013.06.004.

[33] L. Wang, Multibody Dynamics Using Conservation of Momentum with Application to Compliant Offshore Floating Wind Turbines, Ph.D. thesis, Texas A&M University, College Station, TX, USA, 2012.

[34] R. Antonutti, C. Peyrard, L. Johanning, A. Incecik, D. Ingram, An investigation of the effects of wind-induced inclination on floating wind turbine dynamics: heave plate excursion, Ocean. Eng. 91 (2014) 208—217, http://dx.doi.org/10.1016/j.oceaneng.2014.09.008.

[35] R. Antonutti, N. Relun, C. Peyrard, Aerodynamic damping effect on the motions of a vertical-axis floating wind turbine, in: Proc. 14ème Journées de l'Hydrodynamique, Val-de-Reuil, France, 2014.

[36] ASME, 2016 35th International Conference on Ocean, Offshore and Arctic Engineering, online:, 2015 http://www.asmeconferences.org/omae2016/.

[37] ECN, LHEEA — Nemoh, online:, 2014 http://lheea.ec-nantes.fr/doku.php/emo/nemoh/start.

[38] W.E. Cummins, The Impulse Response Function and Ship Motions, Tech. Rep. Report 1661, David Taylor Model Basin, 1962.

[39] T. Ogilvie, Recent progress towards the understanding and prediction of ship motions, in: Proc. of the 6th Symposium on Naval Hydrodynamics, 1964.

[40] J.R. Morison, M.D. O'Brien, J.W. Johnson, S.A. Schaaf, The force exerted by surface waves on piles, Petrol Trans. AIME 189 (1950) 149—154.

[41] T. Sarpkaya, M. Isaacson, Mechanics of Wave Forces on Offshore Structures, Van Nostrand Reinhold Co., New York, USA, 1981.

[42] A. Robertson, J. Jonkman, M. Masciola, H. Song, Definition of the Semi-submersible Floating System for Phase II of OC4, Tech. Rep. NREL/TP-5000—60601, National Renewable Energy Laboratory, 2014.

[43] T. Utsunomiya, H. Matsukuma, S. Minoura, K. Ko, H. Hamamura, O. Kobayashi, I. Sato, Y. Nomoto, K. Yasui, At sea experiment of a hybrid spar for floating offshore wind turbine using 1/10-scale model, J. Offshore Mech. Arctic Eng. 135(3). http://dx.doi.org/10.1115/1.4024148.

[44] T. J. Larsen, T. D. Hanson, A method to avoid negative damped low frequent tower vibrations for a floating, pitch controlled wind turbine, J. Phys. Conf. Ser. 75(1). http://dx.doi.org/10.1088/1742-6596/75/1/012073.

[45] NWTC, Rigid Wind Turbine with Harmonic Motions, online:, 2015 https://wind.nrel.gov/forum/wind/viewtopic.php?f=4&t=831.

[46] M. Philippe, A. Babarit, P. Ferrant, Modes of response of an offshore wind turbine with directional wind and waves, Renew. Energy 49 (2013) 151—155, http://dx.doi.org/10.1016/j.renene.2012.01.042.

[47] P. Blusseau, M.H. Patel, Gyroscopic effects on a large vertical axis wind turbine mounted on a floating structure, Renew. Energy 46 (2012) 31—42, http://dx.doi.org/10.1016/j.renene.2012.02.023.

[48] H. Fujiwara, T. Tsubogo, Y. Nihei, Gyro effect of rotating blades on the floating wind turbine platform in waves, in: Proc. 21st Offshore and Polar Engineering Conference, International Society of Offshore and Polar Engineers, Maui, Hawaii, 2011.

[49] M.D. Masciola, Instructional and Theory Guide to the Mooring Analysis Program, Tech. rep., 2013.

[50] J.M.J. Journée, W.W. Massie, Offshore Hydromechanics, TU Delft, Delft, The Netherlands, 2000.

[51] M. Philippe, Couplages aéro-hydrodynamiques pour l'étude de la tenue à la mer des éoliennes offshore flottantes, Ph.D. thesis, Ecole Centrale de Nantes, Nantes, France, 2012.

[52] J.M. Jonkman, S. Butterfield, W. Musial, G. Scott, Definition of a 5 MW Reference Wind Turbine for Offshore System Development, Tech. Rep. NREL/TP-500—38060, National Renewable Energy Laboratory Golden, CO, USA, 2009.

[53] M. Somerville, GE 3.6 MW Offshore Wind Turbine — 3d Warehouse, online:, 2014 https://3dwarehouse.sketchup.com/user.html?id=0141516218919051828614401.

[54] S. Christiansen, T. Bak, T. Knudsen, Damping wind and wave loads on a floating wind turbine, Energies 6 (8) (2013) 4097—4116, http://dx.doi.org/10.3390/en6084097.

[55] A. Courbois, Etude expérimentale du comportement dynamique d'une éolienne offshore flottante soumise à l'action conjuguée de la houle et du vent, Ph.D. thesis, Ecole Centrale de Nantes, Nantes, France, 2013.